JCTC Journal of Chemical Theory and Computation

Relativistic Effects on the Topology of the Electron Density

Georg Eickerling,[†] Remigius Mastalerz,[†] Verena Herz,[‡] Wolfgang Scherer,*[,‡] Hans-Jörg Himmel,*[,§] and Markus Reiher*[,†]

Laboratorium für Physikalische Chemie, ETH Zurich, Hönggerberg Campus, Wolfgang-Pauli-Strasse 10, CH-8093 Zurich, Switzerland, Institut für Physik, Universität Augsburg, Universitätsstrasse 1, D-86159 Augsburg, Germany, and Institut für Anorganische Chemie, Ruprechts-Karls-Universität Heidelberg, Im Neuenheimer Feld 270, D-69120 Heidelberg, Germany

Received July 16, 2007

Abstract: The topological analysis of electron densities obtained either from X-ray diffraction experiments or from quantum chemical calculations provides detailed insight into the electronic structure of atoms and molecules. Of particular interest is the study of compounds containing (heavy) transition-metal elements, which is still a challenge for experiment as well as from a quantum-chemical point of view. Accurate calculations need to take relativistic effects into account explicitly. Regarding the valence electron density distribution, these effects are often only included indirectly through relativistic effective core potentials. But as different variants of relativistic Hamiltonians have been developed all-electron calculations of heavy elements in combination with various electronic structure methods are feasible. Yet, there exists no systematic study of the topology of the total electron density distribution calculated in different relativistic approximations. In this work we therefore compare relativistic Hamiltonians with respect to their effect on the electron density in terms of a topological analysis. The Hamiltonians chosen are the four-component Dirac−Coulomb, the quasi-relativistic two-component zeroth-order regular approximation, and the scalar-relativistic Douglas−Kroll−Hess operators.

1. Introduction

To base chemical concepts on elements of a quantum mechanical many-electron theory for molecules has a long history. For example, Hinze and Jaffe[1−3] explicated Mulliken's definition of electronegativity[4] in terms of 'orbital electronegativities' and the 'valence state of an atom in a molecule'. For historical reasons, these very successful early conceptual developments were deeply rooted in some sort of molecular-orbital-based picture. In recent years, however, complementary approaches refer to electron density distributions as a central quantity for interpretive studies.[5−8] The study of the topology of the total electron density $\rho(\boldsymbol{r})$ allows a detailed characterization of electronic densities and, within Bader's theory of atoms in molecules,[6] of interatomic interactions. One major advantage of the density-based approaches is that $\rho(\boldsymbol{r})$ is an observable and, hence, available, for instance, from quantum chemical calculations and X-ray or electron diffraction experiments.[9] Owing to the advances in experimental techniques such as low-temperature devices and fast and highly accurate area detectors, high-resolution X-ray diffraction experiments with a subsequent multipolar refinement[10] based on precise, high-resolution X-ray diffraction data became the most convenient experimental technique to analyze the charge density distribution of molecules and solids.[11−15]

The *static* electron density distribution as a physical observable provides a direct linkage between theory and

* Corresponding author e-mail: markus.reiher@phys.chem.ethz.ch (M.R.), wolfgang.scherer@physik.uni-augsburg.de (W.S.), hans-jorg.himmel@aci.uni-heidelberg.de (H.-J.H.).

[†] ETH Zurich.

[‡] Universität Augsburg.

[§] Ruprechts-Karls-Universität Heidelberg.

10.1021/ct7001573 CCC: $37.00
Published on Web 10/20/2007

experiment. This has recently been demonstrated in the case of transition-metal complexes displaying highly unusual structures (e.g., non-VSEPR complexes) or activated bonds as in agostic complexes. Combined studies showed a very good agreement between the charge density distributions obtained from sophisticated quantum-chemical calculations and advanced X-ray studies.[16] Recent studies even allowed the experimental verification of so-called ligand-induced charge concentrations (LICCs) in the valence shell charge concentration of a transition-metal atom[17]—a phenomenon predicted by theory already in 1995.[18] However, the experimental determination of reliable charge density distributions in the case of compounds containing heavy elements (with, say, nuclear charge numbers $Z > 36$) is still a challenge for both theory and experiment. From an experimental point of view the treatment of heavy elements in standard X-ray diffraction techniques is complicated because of the presence of severe absorption in addition to problems arising from extinction, thermal diffuse scattering, Umweganregung (i.e., the Renninger effect which may cause symmetry forbidden reflections to appear in the diffraction pattern due to multiple diffraction within the crystal), thermal motion, and partial structural disorder.[19] The compensation of these experimental error sources requires sophisticated data reduction and correction techniques. Furthermore, experimental studies are difficult because of the small number of valence electrons compared to the large total number of electrons which makes it difficult to describe the small fraction of nonspherically distributed electrons in the valence region within the multipolar model. All of this can be summarized in the suitability factor *S* which is defined as the ratio of the unit cell volume and the sum of the square of the number of core electrons treated spherically symmetric in the multipolar refinements.[20] For crystals of organic molecules, *S* varies typically from 3 to 5, while for first-row transition-metal complexes it is typically lower than 0.3. Accordingly, only a rather small number of experimental studies were carried out on compounds containing transition-metal elements.

On the other hand, quantum chemical calculations, which are used for comparison in many of the experimental studies, often employ effective core potentials to replace the core electrons of the heavy elements. For a direct comparison with experimental results, however, relativistic all-electron calculations [21−23] are needed as a reference—especially for heavy elements. The need of a detailed and thorough *all-electron* analysis employing relativistic Hamiltonians was recently exemplified for the series of $M(C_2H_4)_3$ complexes with M = Ni, Pd, Pt.[24] For this series of complexes we could demonstrate that the shell structure as well as the polarization pattern displaying zones where the charge density is locally concentrated or depleted are quantitatively and even qualitatively different in effective core potential calculations when compared to relativistic all-electron calculations. A careful all-electron analysis of the charge density distribution of these complexes revealed in agreement with previous findings of Kohout, Savin, and Preuss for isolated atoms[25] as well as with the work of Sagar et al.[43] that the negative Laplacian of the charge density distribution fails to recover the complete shell structure. The two outermost shells, i.e., the sixth and fifth shell of Pt, are not resolved while in the case of the 3d and 4d metals, Ni and Pd, respectively, solely the outermost shell is missing. Furthermore, in contrast to the calculations using scalar-relativistic effective core potentials our all-electron calculations employing the scalar-relativistic zeroth-order regular approximation (ZORA) Hamiltonian did also not recover any local zones of charge concentrations and charge depletion in the valence shell of charge concentrations at the Pt center in $Pt(C_2H_4)_3$.[24]

Various relativistic Hamiltonians are nowadays available to include relativistic effects in first-principles calculations. But no systematic study of the effects of these Hamiltonians on the topology of the resulting total electron density exists in the literature. In this work we therefore present the results of a comparative study of calculations on $M(C_2H_2)$ (M = Ni **1**, Pd **2**, Pt **3**) employing several relativistic and quasi-relativistic Hamiltonians, namely the four-component Dirac−Coulomb, the two-component ZORA, and the scalar-relativistic Douglas−Kroll−Hess operators, which are briefly introduced in section 2. Section 3 introduces the computational methodology. We chose a series of homologous complexes as it is well known that relativistic effects increase with the nuclear charge number *Z*.[21−23] For comparison, we also included results calculated with the standard *nonrelativistic* many-electron Hamiltonian which allows us to assess the general magnitude of relativistic effects on the electron density and its topology. After briefly comparing the molecular geometries in section 4, we first discuss the effect of the choice of the Hamiltonian on the topology of the electron density. Although it is sufficient to investigate the role of the Hamiltonian for the most simple approximation to the many-electron wave function, namely for a single Slater determinant in the framework of Hartree−Fock theory, we consider the relative magnitude of electron-correlation effects in section 6 by comparison with density functional theory (DFT) calculations. Finally, in section 7 we discuss the effect of the relativistic approximations on the Laplacian of the electron density. Here we start from the radial Laplacian of isolated atoms and compare its properties to metal atoms bound in the complexes under consideration.

2. Theoretical Background

Within the Hartree−Fock approximation, the *N*-electron wave function is represented by the antisymmetrized product of *N* single-particle functions, the molecular orbitals ϕ_i, which can be written in form of a Slater determinant (*N* is the total number of electrons). This single-determinant wave function will serve as a standard for our comparative study. We thus exclude effects of electron correlation. In section 6, however, we will compare the results of the Hartree−Fock-calculations to a simple model which takes electron correlation effects into account—namely to density functional theory. Although electron correlation is only treated approximately within present-day DFT, this is sufficient for our purpose as we are solely interested in assessing the approximate magnitude of electron correlation compared to relativistic effects on the electron density. The various Hamiltonians used within this study will be briefly introduced in the following subsections.

2.1. Four-Component Methods. In order to systematically study the effect of approximate relativistic Hamiltonians a well-defined reference is of particular importance. The well-established and often called "fully relativistic" reference theory for the description of atoms and molecules in quantum chemistry is based on Dirac's theory of the electron (see ref 26 for a review of these so-called four-component methods). Accordingly, the most appropriate reference Hamiltonian is the Dirac−Coulomb Hamiltonian

$$H_{\mathrm{DC}} = \sum_{i=1}^{N} h_{\mathrm{D}}(i) + \sum_{i=1}^{N}\sum_{j>i}^{N} \frac{1}{r_{ij}} \tag{1}$$

where r_{ij} is the distance of two electrons i and j. Note that we use Hartree atomic units throughout and that we have omitted the nucleus−nucleus repulsion terms for the sake of brevity. The four-component one-electron Dirac operator $h_{\mathrm{D}}(i)$ is given in standard notation as

$$h_{\mathrm{D}}(i) = c\boldsymbol{\alpha}\cdot\boldsymbol{p}_i + (\beta - 1)c^2 - \sum_{A=1}^{M} \frac{Z_A}{R_{iA}} \tag{2}$$

Here, c denotes the speed of light, $\boldsymbol{\alpha}$ represents a 3-vector whose components are (4×4) matrices built from Pauli spin matrices $\boldsymbol{\sigma} = (\sigma_x, \sigma_y, \sigma_z)$ on the off-diagonal, and $\boldsymbol{p}_i$ is the standard linear momentum operator. The second term on the right-hand side of eq 2 contains a shift in energy by the rest energy c^2 (in Hartree atomic units) in order to match the nonrelativistic energy scale. Finally, β is a diagonal (4×4) matrix with $(1, 1, -1, -1)$ entries on the diagonal. The last sum in eq 2 describes the attractive Coulomb interaction between electron i and all nuclei A in the molecule.

Due to the structure of the Dirac operator the one-particle functions in the Slater determinant become four-component molecular spinors

$$\phi_i = \begin{pmatrix} \phi_i^1 \\ \phi_i^2 \\ \phi_i^3 \\ \phi_i^4 \end{pmatrix} \equiv \begin{pmatrix} \phi_i^L \\ \phi_i^S \end{pmatrix} \tag{3}$$

for which we introduced the large and small two-component spinors ϕ_i^L and ϕ_i^S. A one-particle eigenvalue equation for h_{D} can now be written in split notation as

$$(V - \epsilon_i)\phi_i^L + c\boldsymbol{\sigma}\cdot\boldsymbol{p}\phi_i^S = 0 \tag{4}$$

$$c\boldsymbol{\sigma}\cdot p\phi_i^L + (V - 2c^2 - \epsilon_i)\phi_i^S = 0 \tag{5}$$

Within the Hartree−Fock approach chosen here, the N-particle wave function approximated by a Slater determinant Φ provides a total charge density $\rho_{4\mathrm{comp}}(\boldsymbol{r})$ that is a sum over all (occupied) four-component molecular spinors

$$\rho_{4\mathrm{comp}}(\boldsymbol{r}_1) = \int ds_1 \int d\tau_2 \cdots \int d\tau_N \Phi^*(\tau_1,\tau_2,...,\tau_N)\Phi(\tau_1,\tau_2,...,\tau_N)$$
$$= \sum_{i=1}^{N} \phi_i^\dagger(\boldsymbol{r}_1)\phi_i(\boldsymbol{r}_1) = \sum_{i=1}^{N}\sum_{k=1}^{4} \phi_i^{k*}(\boldsymbol{r}_1)\phi_i^k(\boldsymbol{r}_1) \tag{6}$$

where τ_i denotes the set of spatial and spin coordinates $\boldsymbol{r}_i$ and s_i, respectively. In our study, we use this density $\rho_{4\mathrm{comp}}(\boldsymbol{r})$ as the reference density.

2.2. Elimination Techniques. Due to the fact that four-component methods are computationally very demanding, elimination and transformation techniques have been devised in order to decouple the positive- and negative-energy parts of the spectrum of the Dirac Hamiltonian (see ref 27 for a most recent review). These methods aim at a reduction of the four-component Dirac equation to an effective two-component form. In this study we consider two quasi-relativistic Hamiltonians to investigate the effect of such approximations on the topology of the electron density.

One efficient and widely used method to achieve the decoupling of the large and the small components is ZORA.[28−30] Within this approximation one solves eq 5 for ϕ_i^S

$$\phi_i^S = X(\epsilon_i)\phi_i^L \tag{7}$$

where the energy-dependent X-operator reads

$$X(\epsilon_i) = \frac{c\boldsymbol{\sigma}\cdot\boldsymbol{p}}{(\epsilon_i - V + 2c^2)} \tag{8}$$

Inserting $X(\epsilon_i)$ into the upper part of the Dirac equation, namely into eq 4, we obtain

$$(V - \epsilon_i)\phi_i^L + \frac{1}{2c^2}(c\boldsymbol{\sigma}\cdot\boldsymbol{p})\left[\frac{2c^2}{\epsilon_i - V + 2c^2}\right](c\boldsymbol{\sigma}\cdot\boldsymbol{p})\phi_i^L = 0 \tag{9}$$

The resulting expression for the Hamiltonian is energy dependent and can be rewritten and expanded in terms of a Taylor series to finally yield the two-component ZORA Hamiltonian

$$h_{\mathrm{ZORA}} = \boldsymbol{\sigma}\cdot\boldsymbol{p}\frac{2c^2}{2c^2 - V}\boldsymbol{\sigma}\cdot\boldsymbol{p} + V \tag{10}$$

The ZORA Hamiltonian h_{ZORA} is widely used instead of h_{D} of eq 2 for calculations including scalar-relativistic effects as well as spin−orbit coupling.

2.3. Transformation Techniques. The generalized Douglas−Kroll−Hess (DKH) unitary transformation technique[31−33] (see ref 34 for a recent review of conceptual aspects of this theory) aims at a block-diagonalization of the Dirac Hamiltonian resulting in two independent (2×2) matrix operators h_+ and h_- which describe the electronic and the so-called positronic eigenstates, respectively

$$h_{\mathrm{bd}} = Uh_{\mathrm{D}}U^\dagger = \begin{pmatrix} h_+ & 0 \\ 0 & h_- \end{pmatrix} \tag{11}$$

This block-diagonalization can be accomplished by a sequence of unitary transformations

$$h_{\mathrm{bd}} = ...U_3U_2U_1U_0h_{\mathrm{D}}U_0^\dagger U_1^\dagger U_2^\dagger U_3^\dagger... \tag{12}$$

Every U_n in this sequence of unitary transformations is parametrized in terms of a power series expansion of an antihermitian operator W_n,[33] which is chosen to diminish the off-diagonal contributions order by order in the external

potential. According to eq 11 a complete decoupling of the Dirac operator leads to a two-component formulation based on h_+. However, the operator h_+ can be further separated into a one-component spin-free and a spin-dependent part. The DKH approach is most efficient in its scalar-relativistic, spin-free variant, which we chose for this work. We should emphasize that for all non-*p*-block elements of the periodic table of the elements with not too large nuclear charges, $Z \lesssim 100$, spin−orbit coupling does not play a decisive role. This is the reason why we challenge the four-component reference results with scalar-relativistic high-order DKH calculations.

In principle, exact decoupling of the Dirac Hamiltonian would require an infinite number of unitary transformations. However, given a certain accuracy determined by the computational set up (mainly by the quality of the basis set) the expansion may be truncated at a certain order *m*, defining the DKH*m* method.[35] We consider the tenth-order DKH10 Hamiltonian as sufficient for exact decoupling in the scalar-relativistic regime. The order of the DKH operator is related to the *n*th unitary matrix by the so-called $(2n + 1)$-rule. According to this rule, for instance, the tenth-order DKH Hamiltonian is completely defined by the first six unitary matrices U_0, U_1, U_2, U_3, U_4, and U_5. Transformation techniques closely related to the DKH theory which aim at the exact decoupling of the Dirac Hamiltonian such as the infinite-order two-component (IOTC) theory have recently been developed and implemented.[36,37]

2.4. Topological Analysis of the Electron Density. The differences of the densities obtained from calculations employing the Hamiltonians introduced in sections 2.1−2.3 are qualitatively discussed in terms of difference density plots, which directly reveal the change in the spatial distribution of the density. A quantitative measure of the differences is given by the values of $\rho(\boldsymbol{r})$ at a set of characteristic points within the molecule. These points were chosen as the stationary points of the three-dimensional electron density distribution, which are given a special meaning within the theory of atoms in molecules.[6] In particular we analyzed the bond critical points (BCPs) and the ring critical points (RCPs). Within the atoms-in-molecules theory these critical points are classified according to the signs of the eigenvalues of the Hessian matrix which contains the nine second derivatives of $\rho(\boldsymbol{r})$ with respect to the spatial coordinates $\boldsymbol{r} = (x, y, z)$. For example, the atomic positions at which $\rho(\boldsymbol{r})$ adopts maximum values are classified as $(3, -3)$ critical points. Here, (ω, σ) denotes the rank ω, i.e. the number of nonzero eigenvalues and the signature σ which is the sum of the signs of the eigenvalues of the Hessian matrix. Thus, a BCP is classified as a $(3,-1)$ critical point and a RCP as a $(3,+1)$ critical point. Besides this qualitative classification of the critical points the curvature of $\rho(\boldsymbol{r})$ at a bond critical point can be quantitatively characterized utilizing the three eigenvalues of the diagonalized Hessian matrix of $\rho(\boldsymbol{r})$ λ_1, λ_2, and λ_3. The eigenvector belonging to the positive eigenvalue λ_3 points along the bond axis and one can define the bond ellipticity ϵ as[38]

$$\epsilon = \frac{\lambda_1}{\lambda_2} - 1 \tag{13}$$

Here, λ_1 and λ_2 denote the two eigenvalues belonging to the two eigenvectors which span a plane perpendicular to the direction of the bond path and for which $|\lambda_1| \geq |\lambda_2|$ holds. According to this definition, ϵ is always positive. For a rotationally symmetric σ-bond λ_1 and λ_2 are equal and thus $\epsilon = 0$.

Another property sensitive to changes in the topology of the electron density is the topology of the bond path. The bond path is defined for molecules and solids at equilibrium geometry as a set of two gradient lines which originate at the BCP and terminate each at one of the nuclei of a bonded atom pair. Thereby the bond path follows the maximum slope of $\rho(\boldsymbol{r})$ and thus needs not be a straight line but can exhibit a complicated curvy-linear behavior which can be used to characterize the type of a chemical interaction.[39] At this point we should stress that the foundations of the atoms-in-molecules theory have not been rigorously defined in a relativistic four-component theory compared to Schrödinger quantum mechanics.[40] This is, however, no obstacle for our study, because we are interested in the shape of the total electron density, which we simply study in terms of the atoms-in-molecules notation.

In addition to the topology of $\rho(\boldsymbol{r})$, we also analyze the negative Laplacian of the electron density.

$$L(\boldsymbol{r}) = -\nabla^2\rho(\boldsymbol{r}) \tag{14}$$

The Laplacian is the trace of the (3×3) Hessian matrix of $\rho(\boldsymbol{r})$, which is invariant under basis transformations. This definition is convenient, because a *positive* value of $L(\boldsymbol{r})$ corresponds to a region where charge is locally *concentrated* whereas a *negative* sign of $L(\boldsymbol{r})$ corresponds to a region suffering of local charge *depletion*.[6] Analyzing the topology of $L(\boldsymbol{r})$ in the same way as described above for $\rho(\boldsymbol{r})$ provides another set of characteristic (i.e., stationary) points. The local maxima in the negative Laplacian distribution indicate the positions of locally enhanced charge concentration (CC), found within the valence shell of charge concentration ($L(\boldsymbol{r}) > 0$) in the valence region of atoms in molecules. Bader et al. suggested that the outermost shell of CC of an atom (second shell of CC of the carbon atoms and third shell of CC of the nickel atom) represents its (effective) valence shell charge concentration (VSCC).[25,41−46,82]

3. Computational Methodology

The molecular geometries of $M(C_2H_2)$ (M = Ni, Pd, Pt) were taken from a structure optimization with the Turbomole program package[47] employing the BP86 density functional,[48,49] effective core potentials from the Stuttgart group (ecp-10-mdf,[50] ecp-28-mwb,[51] and ecp-60-mwb[51] for Ni, Pd, and Pt, respectively), and basis sets of Gaussian-type functions (GTFs) of triple-ζ plus polarization quality (TZVP) as implemented in Turbomole. The molecular structures obtained from these calculations will be used as default if not explicitly mentioned otherwise, and we will refer to them as **A**. For comparison, we also performed structure optimizations employing all electron TZ2P basis sets of Slater-type

functions (STFs), the BP86 density functional,[48,49] and the scalar-relativistic ZORA approximation using the ADF program package.[52,53] In the following this level of approximation will be denoted **B**.

All four-component Hartree−Fock and DFT as well as the two-component ZORA calculations were performed with the Dirac electronic structure program[54−56] employing completely decontracted basis sets. The density functionals LDA, BLYP, BP86, and B3LYP were chosen as implemented in Dirac.[48,49,57,58] In the cases of Pt and Pd we applied the relativistic quadruple-ζ basis sets devised by Dyall[59,60] in a completely decontracted way, i.e., with all exponents taken as primitive basis functions. This results in the following basis set sizes Pt: (34*s*, 30*p*, 19*d*, 12*f*, 7*g*, 4*h*, 1*i*), Pd: (33*s*, 25*p*, 17*d*, 9*f*, 6*g*, 3*h*). For Ni we supplemented the exponents of the basis set by Pou-Amerigo et al.,[61] which constitutes an expansion of the original basis set by Partridge,[62] by two additional diffuse *h*-type functions with exponents 0.1 and 0.01, yielding a final size of (21*s*, 15*p*, 10*d*, 6*f*, 4*g*, 2*h*). The exponents of Dunning's[63] cc-pVQZ basis set provided the exponents for the lighter elements C and H and result in the following basis set sizes C: (12*s*, 6*p*, 3*d*, 2*f*, 1*g*), H: (6*s*, 3*p*, 2*d*, 1*f*). In view of the overall size of the basis sets used in this study they may well be considered to be close to the basis set limit.

The scalar-relativistic Douglas−Kroll−Hess and the nonrelativistic Hartree−Fock calculations were performed with the Molpro2006.2 program package[64] using the same large primitive basis sets as employed in the four-component calculations. The DKH10 calculations were possible owing to our recent implementation of the arbitrary-order DKH Hamiltonian[65] into the Molpro package.

In each case, the total electron density was then calculated on a cubic grid of points (200 × 200 × 200 points, step size 3 pm). We ensured that the cubic grids were identical in Dirac and Molpro. The search for bond and ring critical points and the determination of the topological parameters was performed using the Integrity program written by P. Rabillier.[66] For unit conversion to eÅ^{-3} and eÅ^{-5}, the results in Hartree atomic units were multiplied with a conversion factor of 6.748315 Å^{-3} and 24.098731 Å^{-5}, respectively. We should note that the explicit multiplication with the elementary charge *e* in the unit would convert the electron density, which is a particle density distribution, into a (positive) electron density distribution of *N* elementary charges. However, this multiplication is hardly made explicit, instead one refers to "eÅ^{-3}" as a fraction of electrons per cubic Ångstrøm. The (negative) *charge* density can be obtained by multiplication of the electron density by −1.

The Laplacian of the total charge density was calculated numerically using a Mathematica[67] routine written by M. Presnitz.[68] The Laplacian, which was then also obtained on a grid of points, was again analyzed using the Integrity program to locate the stationary points.

To assess the error due to the numerical determination of the topological parameters on a grid of points we compared the results of grids with 3 pm and 0.015 pm grid spacing. The values of the electron density at the critical points are the same for both grids. However, the values of the Laplacian at the critical points show some deviations. For example for the C−C bond critical point in complex **1** we find for $L(\boldsymbol{r})$ −26.7 and −26.6 eÅ^{-5} for the grid with 0.03 and 0.015 pm spacing, respectively, which corresponds to a difference of only 0.4%. Only for smaller values of $L(\boldsymbol{r})$ as they are for instance found at the M−C bond critical points, the deviations are somewhat larger. Here we find for compound **1** values of 5.1 and 5.4 eÅ^{-5} using a 0.03 and 0.015 pm grid, respectively. However, these deviations do not affect the result of our study, as we will point out below.

Table 1. BP86 Bond Distances and Angles of M(C_2H_2) (M = Ni, Pd, Pt) in pm and deg as Obtained from the GTF-TZVP Nonrelativistic Calculations (**A**) and the STF-TZ2P ZORA Calculations (**B**)

A	M−C	C−C	C−H	CMC	MCC	MCH
Ni	184.1	128.2	108.5	40.8	69.6	139.6
Pd	204.1	126.5	108.0	36.1	71.9	133.3
Pt	200.5	128.5	108.2	37.4	71.3	135.2
B	M−C	C−C	C−H	CMC	MCC	MCH
Ni	181.1	128.8	108.5	41.7	69.2	139.9
Pd	203.9	126.5	108.0	36.1	71.9	133.5
Pt	198.3	128.7	108.1	37.9	71.1	136.3

Atomic Hartree−Fock calculations on the metal atoms were carried out using a fully numerical four-component (MC)SCF program,[69] in which all angular degrees of freedom are treated analytically, while the two radial functions $F_i(r) = P_i(r)/r$ and $G_i(r) = Q_i(r)/r$ of the 4-spinor are represented on an equidistant (logarithmic) grid of points in the new variable *s*, which is calculated from the radial variable *r* (see ref 70 for details on this type of radial grid).

4. Structural Comparison

The final bond distances and angles obtained from the structure optimizations of **1**−**3** are summarized in Table 1. Comparing the molecular geometries obtained from the GTF-TZVP/nonrel and the STF-TZ2P/ZORA calculations (methods **A** and **B**, respectively), the only significant deviations are found for the M−C bond distances of **1** and **3**, where the differences amount to 3 and 2.2 pm, respectively.

We may compare these generic systems to experimentally known acetylene and ethylene complexes. First of all, the structure of Ni(C_2H_2) agrees well with the one obtained by X-ray diffraction for Ni(C_2H_2)(PPh_3)$_2$ **4**.[71] Due to the C_{2v} symmetry, the two Ni−C distances are equal in **1** (184.1 pm), while for **4** two slightly different bond lengths were found (187.1 and 188.1 pm). The same holds true for the two CCH angles, which are again the same in **1** (150.8°) but differ in **4** (146.8° and 149.4°). The bond distances and angles are also in agreement with those reported earlier on the basis of B3LYP/6-311+G(2d,p) calculations for Ni(C_2H_2) (C−C and C−H distances of 127.6 and 107.8 pm and HCC angles of 148.5°).[72]

The qualitative comparison of the structures for the three generic systems **1**−**3** optimized in both schemes **A** and **B** shows that the C−C bond is less elongated—compared to free acetylene (120 pm)—for **2** (126.5 pm) than for **1** (128.2

Table 2. Values of $\rho(\boldsymbol{r})$ in eÅ^{-3} at the M−C BCPs and at the RCP in Complexes **1**−**3** Using Various Many-Electron Hamiltonians within the Hartree−Fock Approximation for the Total Wave Function[a]

	$\rho(\boldsymbol{r}_{BCP})$	dev	$\rho(\boldsymbol{r}_{RCP})$	dev
	M = Ni			
nonrel	0.97	0.0	0.85	0.0
DKH2	0.97	0.0	0.85	0.0
DKH10	0.97	0.0	0.85	0.0
ZORA	0.97	0.0	0.85	0.0
four-comp	0.97	–	0.85	–
	M = Pd			
nonrel	0.79	1.3	0.76	1.3
DKH2	0.80	0.0	0.78	4.0
DKH10	0.80	0.0	0.78	4.0
ZORA	0.80	0.0	0.78	4.0
four-comp	0.80	–	0.75	–
	M = Pt			
nonrel	0.94	6.0	0.89	4.3
DKH2	1.00	0.0	0.93	0.0
DKH10	1.00	0.0	0.93	0.0
ZORA	1.00	0.0	0.93	0.0
four-comp	1.00	–	0.93	–

[a] In addition the deviations of the values relative to the four-component calculations (dev) are given in %.

Table 3. Values of $L(\boldsymbol{r})$ in eÅ^{-5} and ϵ at the M−C BCPs and $L(\boldsymbol{r})$ at the RCP in Complexes **1**−**3** Using Various Many-Electron Hamiltonians within the Hartree−Fock Approximation for the Total Wave Function[a]

	$L(\boldsymbol{r}_{BCP})$	dev	$\epsilon(\boldsymbol{r}_{BCP})$	dev	$L(\boldsymbol{r}_{RCP})$	dev
	M = Ni					
nonrel	−5.61	7.9	0.28	17.7	−14.28	4.8
DKH2	−4.83	7.1	0.36	5.9	−13.58	0.3
DKH10	−5.09	2.1	0.32	5.9	−13.67	0.4
ZORA	−5.33	2.5	0.29	14.7	−14.11	3.6
four-comp	−5.20	–	0.34	–	−13.62	–
	M = Pd					
nonrel	−6.94	8.4	1.34	22.9	−10.69	2.9
DKH2	−5.91	7.7	1.17	7.3	−9.79	5.8
DKH10	−6.09	4.8	1.20	10.1	−10.42	0.3
ZORA	−6.20	3.1	1.15	5.5	−10.40	0.1
four-comp	−6.40	–	1.09	–	−10.39	–
	M = Pt					
nonrel	−5.88	90.3	0.86	43.3	−11.53	19.5
DKH2	−3.19	3.1	0.61	1.7	−9.54	1.1
DKH10	−3.42	10.7	0.58	3.3	−9.09	5.8
ZORA	−3.29	6.5	0.57	5.0	−9.31	3.5
four-comp	−3.09	–	0.60	–	−9.65	–

[a] In addition the deviations of the values relative to the four-component calculations (dev) are given in %.

pm) and **3** (128.5 pm); only values for scheme A are specified. This is in agreement with experimental results for (d^ippe)M(C_2H_2) (M = Ni **5**, Pt **6**) and (d^ippe)-Pd(C_2PhH) **7** (d^ippe = ^{i}Pr$_2$PCH$_2$CH$_2$P^{i}Pr$_2$) where the shortest C−C bond is also found for **7** (124.6(7) pm, compared to 128.7(7) and 137(3) pm for **5** and **6**, respectively).[73] In previous BP86 calculations on complexes (dpe)M(C_2H_2) (dpe = diphosphinoethane) employing triple-ζ Slater-type basis sets, C−C distances of 127.8, 126.9, and 129.0 pm and MCH angles of 141.0°, 137.4°, and 142.9° for M = Ni, Pd, and Pt, respectively, were found.[74] We note that the C−C bond length as obtained from a standard X-ray diffraction study employing the model of independent atoms for the structure factor refinement turns out to be 6 pm too short compared to results obtained from a multipolar refinement which includes aspherical density contribution due to bond formation.[19] With 49.3 and 46.7 kcal mol^{-1} the ligand dissociation energies for acetylene are similar for M = Ni and Pt. For M = Pd, a smaller value was reported (32.3 kcal mol^{-1}).[74]

5. Choice of the Hamiltonian and Topology of the Electron Density

To analyze the importance of the different Hamiltonians for the resulting electron density $\rho(\boldsymbol{r})$ we employ the Hartree−Fock approximation for the total electronic wave function from which $\rho(\boldsymbol{r})$ is calculated. The results concerning the critical points of the total electron density are summarized in Tables 2 and 3.

Comparing the two extreme cases of densities obtained from calculations with the nonrelativistic and the four-component Dirac−Coulomb Hamiltonian for complexes **1**−**3** one finds that for M = Ni there is no difference in total density at the bond critical point, while for M = Pt it amounts to $\Delta\rho(\boldsymbol{r}_{BCP}) = 0.06$ eÅ^{-3}. Also at the ring critical point the density difference is zero for **1**, while for **3** it is $\Delta\rho(\boldsymbol{r}_{RCP}) = 0.04$ eÅ^{-3}. In the case of M = Pd a small deviation of 0.01 eÅ^{-3} is observed for $\Delta\rho(\boldsymbol{r}_{BCP})$ as well as for $\Delta\rho(\boldsymbol{r}_{RCP})$. These results confirm the expected trend of increasing importance of relativistic corrections when moving from the lighter to the heavier elements in the group.

In order to assess the significance of the deviations found for $\Delta\rho(\boldsymbol{r}_{BCP})$ and $\Delta\rho(\boldsymbol{r}_{RCP})$ in the calculations one can use as reference the estimated standard deviations obtained for the topological parameters from *experimental* charge density studies. As the result of a detailed study concerning the reproducibility of the electron density obtained from high-resolution X-ray diffraction experiments by the International Union of Crystallography in 1984 a mean error in the electron density maps of 0.15 eÅ^{-3} was reported.[75] In recent experimental studies the *estimated standard deviations* for the electron density at the critical points range from 0.01 to 0.05 eÅ^{-3}. These standard deviations are, however, only estimates and are not determined directly from the experimental errors. In the current literature one finds only a few studies concerned with the reproducibility of topological parameters obtained from X-ray experiments.[14] One of these is the comparison of different measurements on glycyl-L-threonine by Lecomte et al.[76] and by Luger et al.[77] which showed that the topological parameters at the critical points agree to 99%, 95%, and 88% for $\rho(\boldsymbol{r}_{BCP})$, $\rho(\boldsymbol{r}_{RCP})$, and $L(\boldsymbol{r}_{BCP})$, respectively.[14] Applying this to the topological parameters of a peptide bond leads to deviations of ∼0.02 eÅ^{-3} and ∼3.0 eÅ^{-5} for the density and the Laplacian at the bond critical points, respectively.[14] Another important matter in this context is the general agreement between experimental and theoretical topological parameters. The various factors which have to be taken into account for such a comparison

were, for instance, recently summarized by Coppens and Volkov.[15] Studies on transition-metal compounds show that the general agreement between experimental and some theoretical values of $\rho(\boldsymbol{r}_{BCP})$ and $L(\boldsymbol{r}_{BCP})$ typically lie in the range of 0.01−0.03 eÅ^{-3} and 0.77−1.13 eÅ^{-5}.[78,79] These values suggest that a deviation of 0.06 eÅ^{-3} found for the $\rho(\boldsymbol{r}_{BCP})$ when including relativistic corrections in complex **3** is indeed significant when comparing results from experiment and from quantum chemical calculations.

Finally the question arises whether the changes of the topological parameters are due to a shift of the positions of the critical points or if they are truly effects of a change in the topology of $\rho(\boldsymbol{r})$. One way to answer this question is to compare the distances of the critical points from the atomic positions for the different Hamiltonians employed. The distances between the M−C bond critical point and M lie in a range between 94.1 and 94.4 pm for M = Ni, 111.9 and 112.0 pm for M = Pd, and 113.0 and 114.0 pm for M = Pt. The corresponding distances between the metal atom and the ring critical point are in a range of 96.1 and 96.2 pm for M = Ni, 111.1 and 111.3 pm for M = Pd, and 113.0 and 113.5 pm for M = Pt. Thus, the changes in the positions of the critical points are small, and the changes in the topological parameters discussed above can clearly be attributed to a change in the topology of $\rho(\boldsymbol{r})$ rather than to a shift in the positions of the critical points.

Comparing densities from all Hamiltonians employed, one finds no effect of the different levels of approximation used for the calculation of the wave function on the values of $\rho(\boldsymbol{r}_{BCP})$ for complex **1** (Table 2). For complex **2** already the DKH2 Hamiltonian gives the same value for $\rho(\boldsymbol{r}_{BCP})$ as is found for the four-component Hamiltonian. Yet, this is not the case for $\rho(\boldsymbol{r}_{RCP})$. While a small deviation of only 1.3% occurs when comparing the nonrelativistic to the four-component result, it increases to 4% for the three other approximate Hamiltonians we included in our study. The scalar-relativistic DKH Hamiltonian as well as the ZORA Hamiltonian including spin−orbit coupling terms overestimate $\rho(\boldsymbol{r}_{RCP})$ by 0.03 eÅ^{-3}. This discrepancy is almost as large as the deviation found between the nonrelativistic and the four-component calculation of complex **3**, where $\Delta\rho(\boldsymbol{r}_{RCP}) = 0.04$ eÅ^{-3}, corresponding to a relative error of 4.3%. In contrast to complex **2**, for M = Pt already the DKH2 Hamiltonian exactly reproduces the value for $\rho(\boldsymbol{r}_{RCP})$ found in the four-component calculation.

Considering the Laplacian of the electron density at the bond and ring critical points as a very sensitive quantity to detect changes in a density distribution, one finds significantly larger relative deviations (see Table 3). Thus, nonrelativistic calculations for complex **1** result in a difference $\Delta L(\boldsymbol{r}_{BCP})$ of 7.9% compared to results from the four-component Hamiltonian. This error is reduced to 7.1% for the DKH2 level of approximation. Only when employing the DKH10 or ZORA Hamiltonian the error is substantially reduced to 2.1% and 2.5%, respectively. However, for $L(\boldsymbol{r}_{RCP})$ the largest deviation is still found for the nonrelativistic Hamiltonian, but for scalar-relativistic DKH2 calculations it is already as low as 0.3%. DKH10 calculations do not reduce the error further, and including spin−orbit effects by applying the ZORA Hamiltonian leads to an increase to 3.6%. Thus, the trend suggested by the values found for $L(\boldsymbol{r}_{BCP})$ cannot be confirmed for $L(\boldsymbol{r}_{RCP})$. A similar situation emerges for the Laplacian at the critical points in the case of complex **2**. Comparatively large deviations of $\Delta L(\boldsymbol{r}_{BCP})$ are found for densities from calculations with the nonrelativistic and the DKH2 Hamiltonian (8.4 and 7.7%, respectively), which are reduced to 4.8 and 3.1% by applying the DKH10 and the ZORA approximations. In this case, $\Delta L(\boldsymbol{r}_{RCP})$ appears to follow the same trend, resulting in remarkably low deviations for the DKH10 and the ZORA Laplacians of only 0.3 and 0.1%.

As expected, the largest error is found for the nonrelativistic calculation for complex **3**, which overestimates the absolute values of $L(\boldsymbol{r}_{BCP})$ by over 90% and $L(\boldsymbol{r}_{RCP})$ by almost 20% relative to the four-component result. These deviations are significantly reduced by the use of any of the relativistic Hamiltonians. The fact that it is the DKH2 Hamiltonian which almost reproduces the values derived from the four-component calculation should not lead to the interpretation that this Hamiltonian is best suited for the description of complex **3** but rather as error compensation between the approximate treatment of scalar- and spin−orbit effects. This can be explained after considering that the DKH10 approach, which includes a more accurate treatment of scalar-relativistic effects, leads to larger deviations compared to the four-component results.

Summarizing these results we conclude that relativistic effects on the topological parameters at the critical points can be observed in complexes **2** and **3**. The deviations of the density at the critical points amount to 1.3% for M = Pd and 6% in the case of M = Pt. Due to the larger variance of the values of the Laplacian of the electron density the relativistic effects are more difficult to quantify based on the data presented in this work. Still it is clear that for complex **3** the values of $L(\boldsymbol{r}_{BCP})$ and $L(\boldsymbol{r}_{RCP})$ are substantially biased if relativistic effects are neglected and that—as it was the case for the density itself—any of the three relativistic Hamiltonians significantly improve the results with respect to the four-component reference calculation.

We note that the magnitude of some of the deviations discussed above are within the error introduced by the use of the finite grid of points for the analysis of the electron density. However, we compare results obtained from the same set of points so that the relative error introduced by the use of a numerical analysis should be small and not relevant for our discussion. As pointed out in section 3 the values of $\rho(\boldsymbol{r})$ do not change with the step size of the grid, and only for small absolute values of $L(\boldsymbol{r})$ a notable deviation is found. Still, this does not affect the main result of our study as especially for complex **3** the errors introduced by neglecting the relativistic effects are much larger than the error due to the use of the finite grid.

The topological parameters discussed so far only provide a very local measure of the relativistic effects on the electron density. Moreover, the largest effect due to relativity is expected within the inner shells of the heavy atoms. The critical points, however, are located in the valence region of the atoms so that one might expect the deviations due to

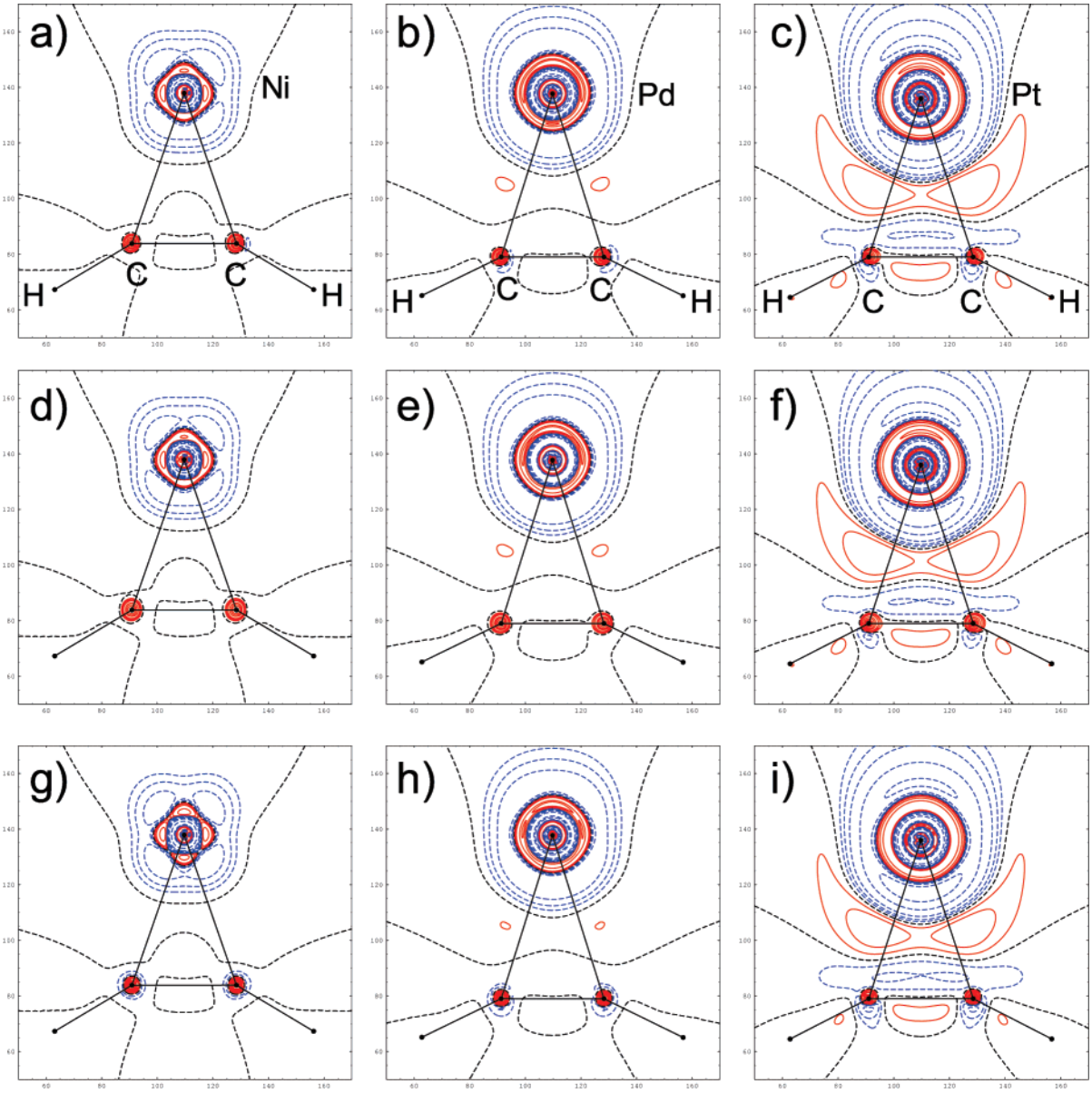

Figure 1. Difference densities in the molecular plane, $\rho_{4comp}(\boldsymbol{r}) - \rho_{nonrel}(\boldsymbol{r})$ for **1** (a), **2** (b) and **3** (c), $\rho_{ZORA}(\boldsymbol{r}) - \rho_{nonrel}(\boldsymbol{r})$ for **1** (d), **2** (e), and **3** (f), $\rho_{DKH10}(\boldsymbol{r}) - \rho_{nonrel}(\boldsymbol{r})$ for **1** (g), **2** (h), and **3** (i). Values of positive and negative difference densities are indicated by solid and dashed lines, respectively. Contour lines are drawn at ± 2, ± 4, $\pm 8 \times 10^n$ eÅ^{-3} with $n = 0, 1, 2$. Note that the axes labels denote grid points.

relativistic effects to be small at these points. To globally assess the differences due to the various levels of approximation used within our study we will now compare difference densities in the molecular plane obtained by subtracting the nonrelativistic densities from the densities obtained from the various relativistic Hamiltonians. Figure 1a),d),g) depicts the differences in the electron density obtained from four-component, ZORA, and DKH10 calculations, respectively, with respect to the nonrelativistic density for complex **1**. Even in the case of the light first transition row element nickel a significant difference is observed. For all three relativistic Hamiltonians four local maxima are found in the difference maps at the nickel atom of which especially the one facing the acetylene ligand is less pronounced in the case of the four-component and ZORA compared to the DKH10 difference map [in the former cases it is smaller than 0.2 eÅ^{-3}, as can be seen by the missing contour line in Figure 1a),d)]. As we will discuss below, the positions of these maxima resemble the positions of the local charge concentrations found in the valence shell of the metal atom. Thus, with relativistic Hamiltonians these regions of local charge concentration should be more pronounced, relative to the nonrelativistic case. In general, the maxima are more pronounced when using the scalar-relativistic DKH10 Hamiltonian compared to the Hamiltonians which include spin−orbit effects. In the case of M = Pd [Figure 1b),e),h)], the difference density maps show a similar scenario compared to **1**. Although weaker, also for complex **2** four maxima can be found in the outer most circular region of positive difference density around the metal atomic nucleus. While the circular maxima and minima can be clearly attributed to the changes in the radial extension of the atomic subshells

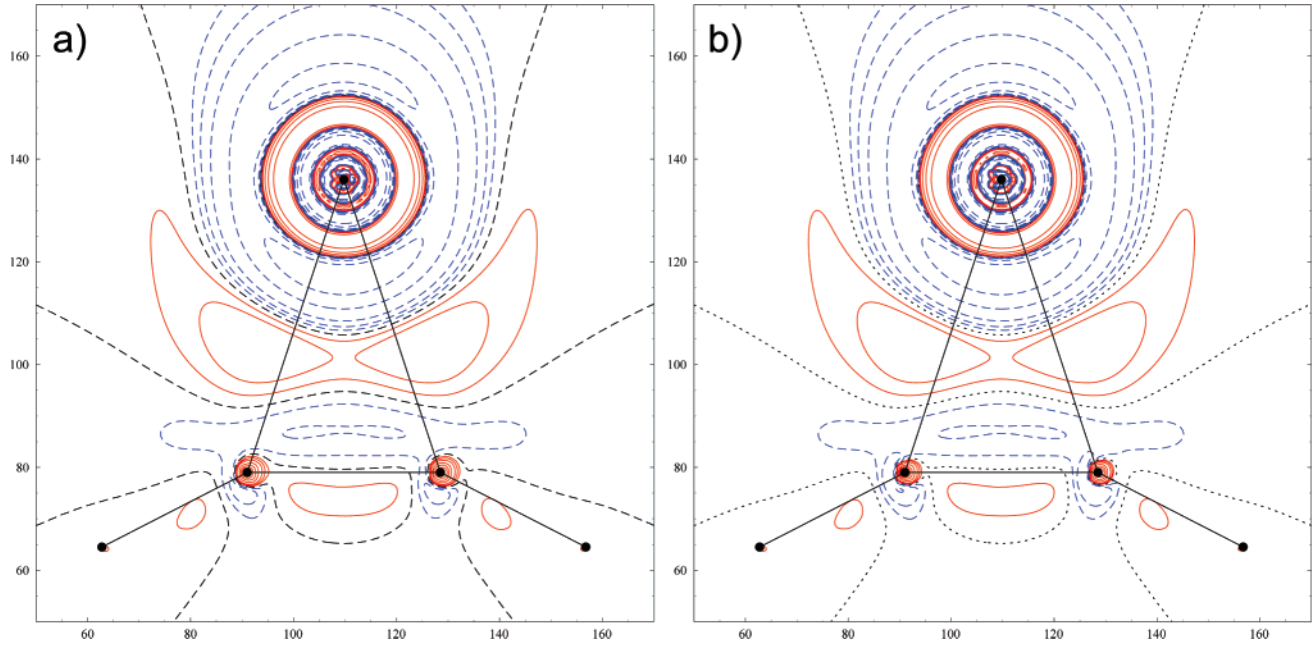

Figure 2. Difference densities in the molecular plane, $\rho_{4comp}(\boldsymbol{r}) - \rho_{nonrel}(\boldsymbol{r})$ for **3** (a), and $\rho^{L}_{4comp}(\boldsymbol{r}) - \rho_{nonrel}(\boldsymbol{r})$ (b). Values of postitive and negative difference densities are indicated by solid and dashed lines, respectively. For the specification of the contour levels see Figure 1. Note that the axes labels denote grid points.

due to scalar relativistic effects, the four local maxima indicate again a change in the electron density in the regions of the local charge concentrations although this is less pronounced in **2**, see below. An additional feature in the difference density maps for complex **2** emerges in the bonding region between the metal atom and the ligand. Two weak maxima appear at positions close to the M−C bond critical points, which are indicative for the small but noticeable relativistic effect on the electron density in the bonding region. This was already noticed above (Table 2) as a difference of 0.01 eÅ^{-3} at the M−C bond critical points.

As expected, the difference density maps for complex **3** [Figure 1c),f),i)] reveal the largest differences for the three metals under consideration in our study. The changes in the radial extension of the subshells again lead to circular maxima and minima around the Pt nucleus position, but here only the ZORA and the four-component difference densities feature one local maximum in the *trans* position to the ligand in the outer most of these positive regions of difference density. The value of 1.4 eÅ^{-3} is significantly larger than the values found for the corresponding local maxima in complexes **1** (0.2 eÅ^{-3}) and **2** (0.4 eÅ^{-3}). The maxima in the metal−ligand bonding region are also more pronounced compared to complex **2** and extend to a much larger region between the Pt atom and the ligand.

Taking into account the result that already the ZORA and the DKH methods are able to reproduce the density obtained from the four-component calculations we finally analyzed the topological changes of the electron density with respect to the contribution of the small components ϕ_i^S of the four-component wave function. As an example Figure 2 depicts the difference densities between the nonrelativistic and the total electron density as obtained from the four-component calculation a) and the corresponding difference considering only the electron density of the large component $\rho^L(\boldsymbol{r})$ b). Due to the local nature of the small component, the differences between both maps are small and only detectable in the close vicinity of the atomic nuclei. Thus the values of $L(\boldsymbol{r})$ at the M−C bond critical point and at the ring critical point differ only by 3.9 and 4.1%, while the values of $\rho(\boldsymbol{r})$ remain unchanged. This is the reason why the two-component methods which do not completely eliminate the small component are still able to account for most of the relativistic effects on the topology of the electron density.

In summary, comparing the overall topology of the difference density maps presented in Figure 1 we note several points: (i) The differences between the nonrelativistic and the relativistic densities increase with the nuclear charge Z of the metal atom from the 10th group of the periodic table. (ii) The differences in the absolute values of $\rho(\boldsymbol{r})$ reach values of more than 1 eÅ^{-3} in the valence region of the platinum atom. (iii) The overall changes in the electron density due to relativistic effects in compounds **1**−**3** are already well accounted for by the scalar-relativistic DKH10 Hamiltonian. (iv) Inclusion of spin−orbit effects by the two-component ZORA approximation does not improve on the DKH10 results when compared to the four-component reference.

6. Effect of Electron Correlation on the Topology of the Electron Density

In order to assess the importance of relativistic effects on the total electron density in relation to electron correlation effects, we compare results from the Dirac−Coulomb Hamiltonian in Hartree−Fock calculations (abbreviated Dirac−Hartree−Fock in the following) with those obtained by four-component Kohn−Sham DFT calculations using various density functionals. The results are summarized in Table 4.

For all three different BCPs present in complex **1** the Dirac−Hartree−Fock approximation overestimates the value

Table 4. Values of $\rho(\boldsymbol{r})$ in eÅ^{-3} at the Bond and Ring Critical Points of **1**−**3** Obtained from Four-Component Calculations Using Various Different Density Functionals[a]

	Ni		Pd		Pt	
	$\rho(\boldsymbol{r})$	dev	$\rho(\boldsymbol{r})$	dev	$\rho(\boldsymbol{r})$	dev
			M−C			
DHF	0.97	–	0.80	–	1.00	–
LDA	0.95	2.1	0.80	0.0	0.98	2.0
BLYP	0.94	3.1	0.79	1.3	0.97	3.0
BP86	0.94	3.1	0.79	1.3	0.97	3.0
B3LYP	0.94	3.1	0.79	1.3	0.98	2.0
			C−C			
DHF	2.56	–	2.64	–	2.56	–
LDA	2.50	2.3	2.59	1.9	2.50	2.3
BLYP	2.53	1.2	2.62	0.8	2.53	1.2
BP86	2.52	1.6	2.61	1.1	2.52	1.6
B3LYP	2.53	1.2	2.62	0.8	2.54	0.8
			C−H			
DHF	1.96	–	1.99	–	1.99	–
LDA	1.87	4.6	1.89	5.0	1.90	4.5
BLYP	1.91	2.6	1.94	2.5	1.94	2.5
BP86	1.92	2.0	1.94	2.5	1.95	2.0
B3LYP	1.92	2.0	1.95	2.0	1.95	2.0
			RCP			
DHF	0.85	–	0.78	–	0.93	–
LDA	0.91	7.1	0.78	0.0	0.93	0.0
BLYP	0.89	4.7	0.76	2.6	0.91	2.2
BP86	0.90	5.9	0.77	1.3	0.92	1.1
B3LYP	0.89	4.7	0.77	1.3	0.92	1.1

[a] The relative deviation (dev) in % is given with respect to the results of the Dirac−Hartree−Fock (DHF) calculation.

of $\rho(\boldsymbol{r})$ and at the ring critical point it underestimates $\rho(\boldsymbol{r})$ compared to the DFT results. The largest deviations, 7.1% for the local density approximation (LDA) and 5.1% for the generalized gradient approximation (GGA) functionals (like BLYP, BP86, B3LYP), are found for $\rho(\boldsymbol{r})$ at the ring critical point (deviations given relative to the DHF results). The bond path profile is found to be V-shaped for all cases, but the path is found to be more exocyclic in the case of the Dirac−Hartree−Fock calculations, indicated by the distance between the M−C BCPs of 81.8 pm for Dirac−Hartree−Fock compared to 62.1 pm for the LDA and 66.0 pm for the GGA functionals.

In the case of complex **2** there is no clear trend found for the effect of the various different functionals used as it was the case for M = Ni. The values for $\rho(\boldsymbol{r})$ at the M−C bond critical points are the same comparing the Dirac−Hartree−Fock and the LDA results and only 0.01 eÅ^{-3} higher than those obtained with the GGA functionals. The same holds true for $\rho(\boldsymbol{r})$ at the ring critical points, where the deviations are also remarkably small (same values for Dirac−Hartree−Fock and LDA, 1.7% difference (averaged values) between Dirac−Hartree−Fock and GGA). Only for the C−C and the C−H bonds $\rho(\boldsymbol{r})$ at the bond critical points is again overestimated by the Dirac−Hartree−Fock calculation (LDA: 1.9%, 5.0%; GGA: 0.9%, 2.3% for the C−C and the C−H bond, respectively). The profile of the bond path is again V-shaped in all cases, as it was the case for M = Ni. It is found to be more endocyclic in the DFT calculations (d(M−C BCP) = 67.2, 60.5, and 64.1 pm for Dirac−Hartree−Fock, LDA, and GGA, respectively). However, the difference between the Dirac−Hartree−Fock and the GGA results is significantly smaller for M = Pd (3.1 pm) compared to M = Ni (15.8 pm).

For **3** the same trend for $\rho(\boldsymbol{r})$ at the bond critical points is found as in the case of M = Ni. Dirac−Hartree−Fock overestimates the values compared to the four-component DFT results. But for M = Pt, the values of $\rho(\boldsymbol{r})$ at the ring critical point are very similar for all cases. As for Ni and Pd, the bond path profile is always V-shaped and more endocyclic for the DFT calculations (distances between the M−C bond critical points d(M−C BCP) = 78.2, 71.1, and 73.8 pm for Dirac−Hartree−Fock, LDA, and GGA, respectively). The difference between the Dirac−Hartree−Fock and the GGA results is again small (4.4 pm).

To conclude, the inclusion of electron correlation within DFT leads to reduced values of $\rho(\boldsymbol{r})$ at the bond critical points of the C−C and C−H bonds for all complexes. The same holds true for the M−C bond in the case of M = Ni and Pt. This indicates that the very good agreement of $\rho(\boldsymbol{r})$ at the critical points between the Dirac−Hartree−Fock and the DFT calculations for M = Pd is due to a cancellation of two complementary effects. The qualitative nature of the topology (i.e., V-shaped bond path profile) is not affected by the inclusion of electron correlation, though it still leads to a change in the curvature of the bond path profile. These results are in agreement with earlier studies that investigated the effects of electron correlation on the topology of the electron density.[80] If we assume that no artifacts are introduced through the approximate exchange functional, then the effect on the topology of $\rho(\boldsymbol{r})$ as exerted by electron correlation is comparable in magnitude to the effects found for the different relativistic Hamiltonians discussed above.

7. The Laplacian of the Electron Density

Up to now only the topology of $\rho(\boldsymbol{r})$ has been discussed in detail. The analysis of the Laplacian of the total electron density and — as already mentioned in section 5 — of the local charge concentrations found in the valence shell of charge concentrations of the metal atoms should provide detailed insight into the relativistic effect on $\rho(\boldsymbol{r})$. As was shown by Shi and Boyd[81] and by Sagar et al.[43] for nonrelativistic wave functions and later by Kohout, Savin, and Preuss[25] by relativistic calculations on isolated third-row transition-metal atoms the shell structure of *isolated* atoms is not completely resolved by the Laplacian. For light main group elements regions of positive and negative values of $L(\boldsymbol{r})$ found for each subshell are clearly distinguishable. Starting with the transargonic elements the fourth shell of charge concentration is already so weakly visible in $L(\boldsymbol{r})$ that it might only appear as a small shoulder in the *negative* region of $L(\boldsymbol{r})$.[82] For third-row transition-metals, no maximum for the $n = 6$ shell could be found at all (with n being the principle quantum number).

In the following we will discuss to what extent these earlier findings on isolated atoms are transferable to the transition-metal complexes **1**−**3**. As in the case of the M(C_2H_2) molecules, we solely rely on a decomposition of the total

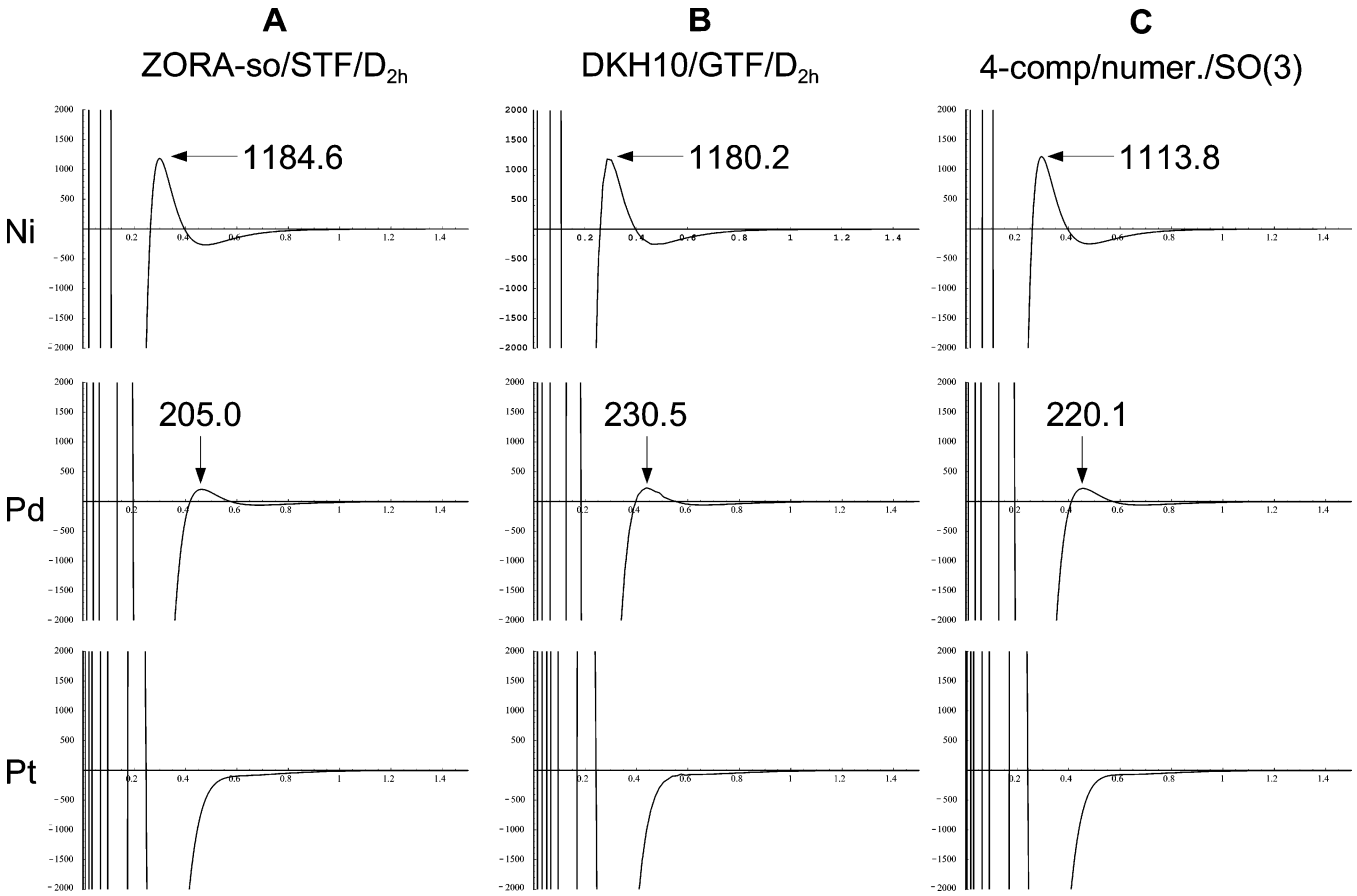

Figure 3. Comparison of $L(\boldsymbol{r})$ (in eÅ^{-5}) for an isolated Ni, Pd, and Pt atom as obtained from a quasi two-component ZORA calculation (D_{2h} symmetry) using a triple-ζ basis set of Slater functions (STF) (A), a scalar relativistic DKH10 calculation (D_{2h} symmetry) using a GTF basis set (B) and a fully numerical four-component calculation of a pure $ns^0(n-1)d^{10}$ configuration (in radial SO(3) symmetry) (C).

electron density of an isolated atom in terms of the orbitals of a single configuration. Consequently, we again adopt the Hartree−Fock model also for the atomic calculations and hence consider only the singlet configuration $ns^0(n-1)d^{10}$. We first analyze the spherically averaged density obtained from a four-component Hartree−Fock calculation using a fully numerical code where the atomic 4-spinors in the Slater determinant are given by

$$\phi_{n_i,\kappa_i,m_{j(i)}}(r,\vartheta,\varphi)=\begin{pmatrix}F_i(r) & \chi_{\kappa_i,m_{j(i)}}(\vartheta,\varphi)\\ \mathrm{i}G_i(r) & \chi_{-\kappa_i,m_{j(i)}}(\vartheta,\varphi)\end{pmatrix} \qquad (15)$$

The radial averaged density $\bar{\rho}(\boldsymbol{r})$ is then subjected to the action of the Laplacian operator transformed from Cartesian coordinates to spherical coordinates which then reads[43]

$$\Delta(x,y,z)\rightarrow\Delta(r,\vartheta,\varphi)\rightarrow\Delta(r)=\frac{\partial^2}{\partial r^2}+\frac{2}{r}\frac{\partial}{\partial r} \qquad (16)$$

The $L(\boldsymbol{r})$ maps obtained for a nickel, palladium, and a platinum atom are shown in Figure 3C. Starting at $r=0$ $L(\boldsymbol{r})$ is positive infinite.[43] According to Bader[42] we count the first zero-crossing as the first shell. The total of five zero-crossings can be attributed to three clearly distinguishable shells in the case of the nickel atom. Moving to the heavier palladium atom, an analogous scenario emerges. Here, the seven zero-crossings indicate four resolved subshells in $L(\boldsymbol{r})$. Yet, the maximum in the Laplacian indicative for the outermost shell is significantly weakened compared to the lighter nickel atom (220.1 and 1113.8 eÅ^{-5}, respectively). For platinum the fifth shell is even less pronounced, and thus only a very weak maximum is found (6.8 eÅ^{-5}). This trend is also observed when instead of the four-component Hamiltonian the ZORA or the DKH10 approximation is applied (Figure 3, parts A and B, respectively). The absolute values found for the maxima in $L(\boldsymbol{r})$ corresponding to the outermost shell are similar for all three model Hamiltonians in the case of nickel and palladium. In the case of platinum no maximum to be attributed to the fifth shell is found for any of the calculations employing either the ZORA, the DKH10, or the four-component Hamiltonian.

Turning from the Laplacian of the isolated metal atoms to the molecular systems **1**−**3** Figure 4 depicts the Laplacian along a line perpendicular to the C−C bonding axis moving from the metal atom toward the C−C BCP of the acetylene ligand. In Figure 4a,b the Laplacian as obtained from calculation using the nonrelativistic, the DKH10, the ZORA, and the four-component Hamiltonian are compared. As was already the case for the density and the Laplacian at the critical points no significant difference can be observed for complex **1**. Only in complex **3** a significant difference is found. Here, the nonrelativistic calculations reveal two weak maxima in the negative region of $L(\boldsymbol{r})$ at approximately 0.75

Å from the nucleus (−3.36 and −3.55 eÅ^{-5} for the maximum facing and opposite to the ligand, respectively). These maxima are not observed when any of the three relativistic Hamiltonians considered within our study is used. In addition, in the relativistic calculation the electron density in the region of the valence shell cis to the ligand appears to be less concentrated than in the region trans to the ligand, which is not the case for the nonrelativistic Laplacians. Thus, in general the result found for the isolated atoms, namely the diminishing of the valence shell charge concentration starting from the second transition-metal period, is also found for metal atoms bound in molecules. The region of charge concentration which can be attributed to the valence shell of a first transition row atom is less pronounced in second-row transition metals and finally reduced to a weak maximum in the *negative* region of $L(\boldsymbol{r})$ in the case of nonrelativistic calculations. For isolated atoms relativistic effects can change the situation qualitatively and cause a valence shell still to be observed as was shown by the *positive* value of $L(\boldsymbol{r})$ in the valence region of the platinum atom. Yet, for the Pt atom bound to a ligand in **3** the opposite effect is observed, and the subtle maximum in the negative region of $L(\boldsymbol{r})$ which is found in the nonrelativistic calculation vanishes in the relativistic calculations.

Finally we will now compare the overall topology of $L(\boldsymbol{r})$ in the molecular plane of complexes **1**−**3** as obtained from the calculations using the different relativistic Hamiltonians (see Figure 5). Beginning again with **1** for which $L(\boldsymbol{r})$ is shown in Figure 5a),d),g),j) for the four-component, the ZORA, the DKH10, and the nonrelativistic Hamiltonian, respectively, no differences are observed at first sight. For all cases, four ligand induced charge concentrations[82] are found in the valence region of the nickel atom, LICC1 facing the acetylene ligand, LICC2 (and the symmetry equivalent LICC2′) on a line parallel to the C−C bond axis, and LICC3 opposite to the ligand. The origin of this polarization was recently investigated within an experimental study on the nickel complex [Ni(C_2H_4)dbpe] (dbpe = $Bu^t_2PCH_2CH_2PBu^t_2$).[39] There it was shown that the occurrence of the four ligand induced charge concentrations in the MCC plane of the valence shell of the metal atom can directly be attributed to the π back-donation of electron density from the occupied metal *d* orbitals to the empty π^* orbitals of the ligand. The positions of LICC1-4 resemble that of the maxima found in the difference densities discussed in section 5. The values of $L(\boldsymbol{r})$ and $\rho(\boldsymbol{r})$ at the positions of the ligand induced charge concentrations are given in Table 5. The first thing we note is that the values of $L(\boldsymbol{r})$ are generally reduced by about a factor of 2 compared to the values found for the valence shell of the isolated nickel atom (600 compared to 1100 eÅ^{-5}). Closer inspection of the values for the three different local charge concentrations reveals an increase relative to the nonrelativistic calculation in the value of $L(\boldsymbol{r})$ for LICC1 by 30, 25, and 24 eÅ^{-5} using the DKH10, the ZORA, and the four-component Hamiltonian, respectively. A similar increase of 25 and 21 eÅ^{-5} (averaged values) is observed for the two charge concentrations denoted as LICC2 and LICC3, respectively. Thus, even in the case of the lightest of the metal atoms considered within our study,

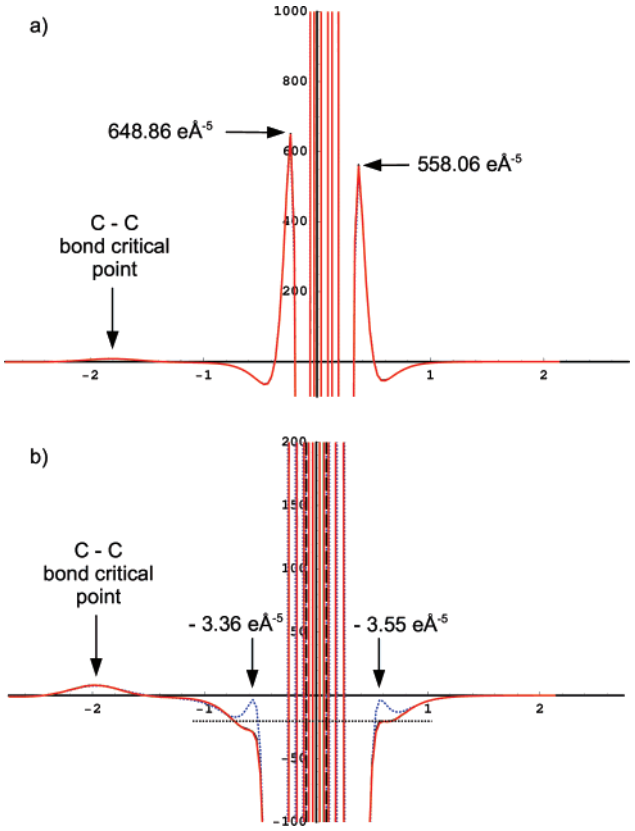

Figure 4. Comparison of $L(\boldsymbol{r})$ (in eÅ^{-5}) along a line through the metal atom position and the C−C bond critical point of the acetylene ligand in complexes a) **1** and b) **3**. The dotted and solid lines represent the nonrelativistic and the relativistic Hamiltonians, respectively. Note the different scales for the *y*-axis in a) ($L(\boldsymbol{r})_{max}$ = 1000 eÅ^{-5}) and b) ($L(\boldsymbol{r})_{max}$ = 200 eÅ^{-5}). The values marked in a) are referring to the four-component calculation, while in b) they refer to the nonrelativistic calculation.

Table 5. Values of $L(\boldsymbol{r})$ in eÅ^{-5} and $\rho(\boldsymbol{r})$ in eÅ^{-3} at the Positions of the Ligand Induced Charge Concentrations (LICC) in Complexes **1** and **2**, i.e. for M(C_2H_2) with M = Ni and M = Pd, Respectively

	$L(\boldsymbol{r}_{LICC})$			$\rho(\boldsymbol{r}_{LICC})$		
	LICC1	LICC2	LICC3	LICC1	LICC2	LICC3
			M = Ni			
nonrel	642	612	544	39.76	38.25	36.77
DKH10	672	639	567	40.28	38.79	37.37
ZORA	667	637	565	40.04	39.66	38.36
four-comp	666	636	563	40.16	38.76	37.28
			M = Pd			
nonrel	85	80	74	13.11	12.54	12.41
DKH10	81	77	74	13.29	12.79	12.73
ZORA	81	76	73	13.32	12.82	12.71
four-comp	82	76	73	13.32	12.81	12.71

relativistic effects on the magnitude of the local charge concentrations are clearly observable. As was already discussed in section 5 by means of the difference density maps, the increase of charge concentration in these regions is at the same time accompanied by an increase in the values of $\rho(\boldsymbol{r})$ (Table 5). For complex **2**, the inspection of the

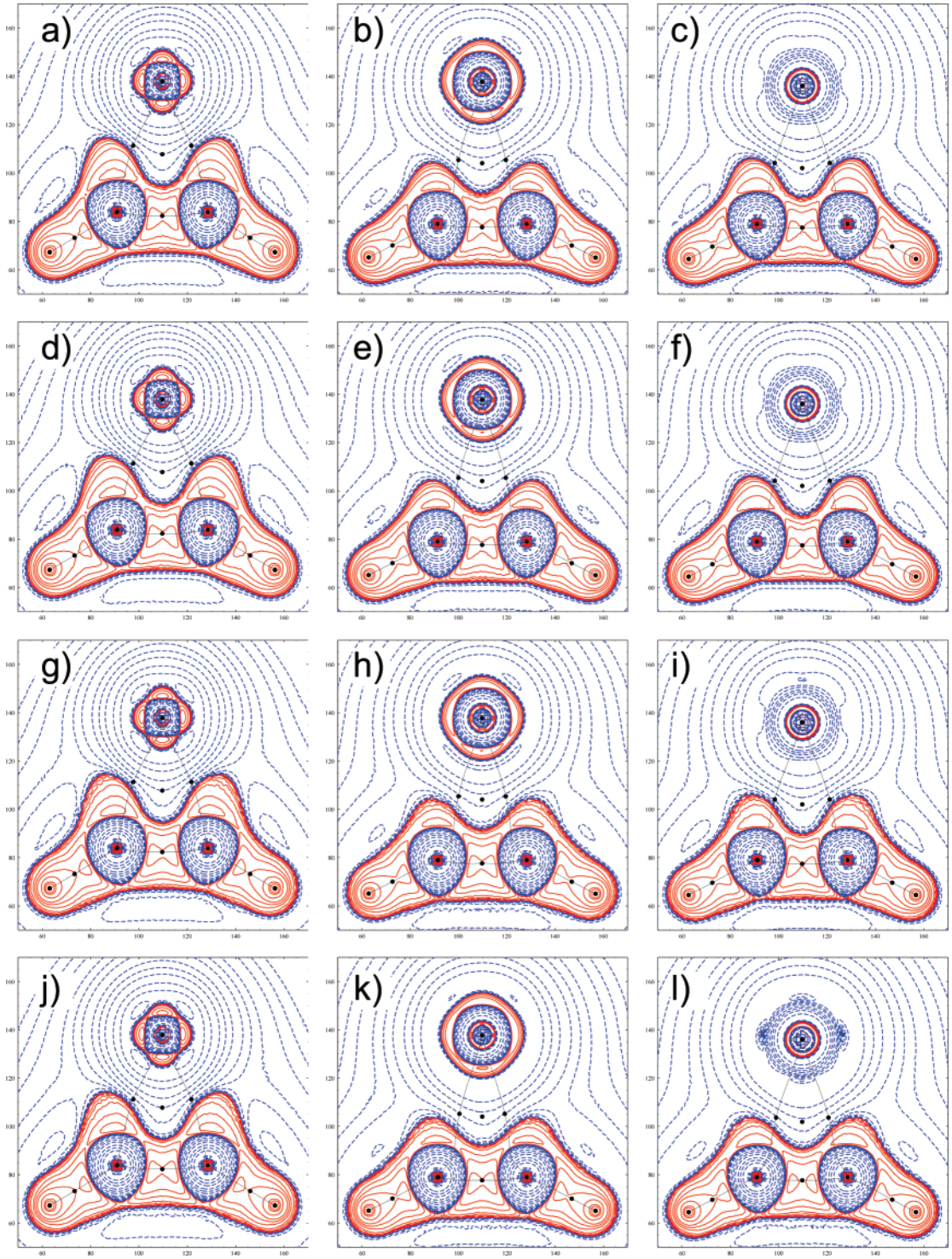

Figure 5. *L*(***r***) in the molecular plane of complexes **1**−**3** as obtained from four-component (a−c), ZORA (d−f), DKH10 (g−i), and nonrelativistic (j−l) calculations. Positive and negative values of *L*(***r***) are denoted by solid and dashed lines, respectively, and the bond paths are drawn as black solid lines. The positions of the critical points are indicated by filled black circles. The contour lines are drawn at the default values specified in Figure 1.

Laplacian maps in Figure 5b),e),h),k) shows no qualitative differences similar to the situation for **1**. In the case of M = Pd there is (relative to the absolute values) a similar change in the values of $L(\boldsymbol{r})$ at the positions of the ligand induced charge concentrations (Table 5) as was found for complex **1** (approximately 5%). The absolute values of $L(\boldsymbol{r})$ at the positions of the local concentrations are significantly smaller, as already discussed above, and only for LICC1 and LICC2 a decrease by approximately 4 eÅ^{-5} is observed when comparing the different relativistic Hamiltonians to the nonrelativistic case. In addition, there is a slight increase in the values of $\rho(\boldsymbol{r})$ at the positions of the local charge concentrations, as was the case for complex **1**. The significantly smaller values of $\rho(\boldsymbol{r})$ at the positions of the ligand induced charge concentrations in **2** compared to **1** are due to the fact that the distance between the nucleus and the local

maxima in $L(\boldsymbol{r})$ is larger for **2** (0.46 Å) than for **1** (0.28 Å). At these distances to the nucleus the values of $\rho(\boldsymbol{r})$ as obtained by numerical four-component calculations on the free atoms are 36.07 eÅ^{-3} for the nickel and 12.28 eÅ^{-3} for the palladium atom, which in both cases is close to the values found for the positions of the local charge concentrations in **1** and **2**. Comparing finally $L(\boldsymbol{r})$ in the molecular plane of complex **3** [Figure 5c),f),i),l)] one finds a significant difference between the nonrelativistic and the relativistic calculations but again no change between the three relativistic Hamiltonians. As already indicated by the radial plots of $L(\boldsymbol{r})$ in Figure 4, local maxima in the negative region around the platinum atom are found when using the nonrelativistic Hamiltonian. The positions and distances to the nucleus closely resemble the positions of the ligand induced charge concentrations found for **2**. These maxima are not found with the relativistic Hamiltonians. Apart from this there are no significant differences in the topology of $L(\boldsymbol{r})$.

8. Summary and Conclusion

In this work we conducted a systematic study of relativistic effects on the total electron density. We also compared these effects to those due to electron correlation. In this way, we were able to assess theory-inherent deficiencies in electron density studies. This is important because so far experimental and calculated densities have been compared directly neglecting the fact that both are affected by measurement errors and by a method-inherent error, respectively. Hence, hardly any reliable error estimates are available for either experiment or theory. One aim of the present study was to close this gap for the theoretical approaches. We should, however, note that we did not investigate the magnitude of method-inherent errors as introduced by a small-sized basis set (since our results were obtained close to the basis set limit; compare also refs 14, 15, 83, and 84 in this context) or by the fact that the study of an isolated molecule does not necessarily represent a true benchmark for X-ray diffraction studies of molecular crystals.

While scalar-relativistic effects were included through DKH Hamiltonians, spin−orbit effects were included in the ZORA framework. Results from these calculations were compared to the limiting reference cases, namely to nonrelativistic and four-component results. We could show that especially for the platinum complex **3** the differences in the topological parameters at the critical points and thus even in the bonding region due to relativistic effects are of significant magnitude when comparing results obtained from experimental and theoretical electron densities. This is best illustrated by the difference in $\rho(\boldsymbol{r})$ at the M−C bond critical point in **3** which is underestimated by 0.06 eÅ^{-3} (corresponding to a relative deviation of 6%) when a nonrelativistic Hamiltonian is employed compared to the four-component result.

The comparison of the electron densities obtained from calculations employing the DKH, ZORA, and the Dirac−Hartree−Fock Hamiltonian suggests, however, that the relativistic effects in complexes **1**−**3** are already accounted for by a scalar-relativistic approximation, so that computationally more demanding two-component calculations including spin−orbit effects or even four-component calculations are not necessarily required. The corresponding deviations in the Laplacian can be much larger (up to 90% for $L(\boldsymbol{r}_{BCP})$ in complex **3**). This fact again demonstrates how the Laplacian can be employed to detect subtle changes in an electron density distribution. A detailed analysis of the Laplacian and especially of the local charge concentrations of complexes **1** and **2** showed that the scalar relativistic contraction of the electronic core shells of the metal atoms leads to an increase in $L(\boldsymbol{r})$ as well as in $\rho(\boldsymbol{r})$ at the positions of the local charge concentrations. Yet, as we demonstrated by a detailed analysis of the electronic shell structure of the isolated atoms and the metal centers in the complexes **1**−**3** the vanishing outer most shell as revealed by the Laplacian plays the far greater role when comparing the topology of the Laplacian within the 10th group of the periodic table.

Finally, comparing results obtained within the Hartree−Fock approximation to results obtained from DFT calculations for complexes **1**−**3** we could show that the effect of electron correlation on the topology of the electron density as accounted for within present-day density functional theory (up to 5.9% change in $\rho(\boldsymbol{r})$ at the M−C bond critical point in complex **1**) can be of the same order of magnitude as the relativistic effects.

Acknowledgment. This project has been generously supported by the German Science Foundation DFG (SPP 1178 "Experimental Electron Density as a Key to the Understanding of Chemical Interactions"). It is a pleasure for M.R. to gratefully acknowledge that it was made possible by the German Science Foundation DFG to continue funding (through Re1703/2-1) in Switzerland after the relocation of M.R. from Jena to Zurich. V.H. thanks NanoCat, an International Graduate Program within the Elitenetzwerk Bayern for financial support. This paper is dedicated to Professor Juergen Hinze, Ph.D., on the occasion of his 70th birthday.

References

(1) Hinze, J.; Jaffé, H. H. *J. Am. Chem. Soc.* **1962**, *84*, 540−546.

(2) Hinze, J.; Jaffé, H. H. *Can. J. Chem.* **1963**, *41*, 1315−1328.

(3) Hinze, J.; Jaffé, H. H. *J. Phys. Chem.* **1963**, *67*, 1501−1506.

(4) Mulliken, R. S. *J. Chem. Phys* **1934**, *2*, 782−793.

(5) Parr, R. G. *J. Chem. Phys* **1978**, *68*, 3801−3807.

(6) Bader, R. *Atoms in Molecules;* Clarendon Press: Oxford, 1990.

(7) Geerlings, P.; DeProft, F.; Langenaeker, W. *Chem. Rev.* **2003**, *103*, 1793−1873.

(8) Ayers, P. *Faraday Discuss.* **2007**, *135*, 161−190.

(9) Zuo, J. M.; Kim, M.; O'Keeffe, M.; Spence, J. C. H. *Nature* **1999**, *401*, 49−52.

(10) Hansen, N. K.; Coppens, P. *Acta Crystallogr., Sect. A: Found. Crystallogr.* **1978**, *34*, 909−921.

(11) Coppens, P. *X-Ray Charge Densities and Chemical Bonding;* Oxford University Press: Oxford, New York, 1997.

(12) Gatti, C. *Z. Kristallogr.* **2005**, *220*, 399−457.

(13) Tsirelson, V. G.; Ozerov, R. P. *Electron Density and Bonding in Crystals;* Institute of Physics Publishing: Bristol, 1996.

(14) Koritsanszky, T. S.; Coppens, P. *Chem. Rev.* **2001**, *101*, 1583−1627.

(15) Coppens, P.; Volkov, A. *Acta Crystallogr., Sect. A: Found. Crystallogr.* **2004**, *A60*, 357−364.

(16) Scherer, W.; McGrady, G. S. *Angew. Chem., Int. Ed.* **2004**, *43*, 1782−1806.

(17) Scherer, W.; Sirsch, P.; Shorokhov, D.; Tafipolsky, M.; McGrady, G. S.; Gullo, E. *Chem. Eur. J.* **2003**, *9*, 6057−6070.

(18) Byetheway, I.; Gillespie, R. J.; Tang, T. H.; Bader, R. F. W. *Inorg. Chem.* **1995**, *34*, 2407−2414.

(19) Reisinger, A.; Trapp, N.; Krossing, I.; Altmannshofer, S.; Herz, V.; Presnitz, M.; Scherer, W. *Angew. Chem.* **2007**, in press.

(20) Stevens, E. D.; Coppens, P. *Acta Crystallogr., Sect. A: Found. Crystallogr.* **1976**, *32*, 915−917.

(21) Schwerdtfeger, P. *Relativistic Electronic Structure Theory. Part I. Fundamentals;* Elsevier: Amsterdam, 2002.

(22) Schwerdtfeger, P. *Relativistic Electronic Structure Theory. Part II. Applications;* Elsevier: Amsterdam, 2004.

(23) Hess, B. A. *Relativistic Effects in Heavy-Element Chemistry and Physics;* Wiley: Chichester, 2003.

(24) Hebben, N.; Himmel, H.-J.; Eickerling, G.; Herrmann, C.; Reiher, M.; Herz, V.; Presnitz, M.; Scherer, W. *Chem. Eur. J.* **2007**, DOI: 10.1002/chem.200700885.

(25) Kohout, M.; Savin, A.; Preuss, H. *J. Chem. Phys.* **1991**, *95*, 1928−1942.

(26) Reiher, M.; Hinze, J. Four-component ab initio Methods for Electronic Structure Calculations of Atoms, Molecules and Solids. In *Relativistic Effects in Heavy-Element Chemistry and Physics;* Wiley-VCH: Weinheim, 2003; pp 61−88.

(27) Reiher, M.; Wolf, A.; Hess, B. A. Relativistic Quantum Chemistry: From quantum electrodynamics to quasi-relativistic methods. In *Handbook of Theoretical and Computational Nanotechnology*; Rieth, M., Schommers, W., Eds.; 2006; Vol. 1, pp 401−444.

(28) Chang, C.; Pelissier, M.; Durand, P. *Phys. Scr.* **1986**, *34*, 394−404.

(29) van Lenthe, E.; Baerends, E.-J.; Snijders, J. G. *J. Chem. Phys.* **1993**, *99*, 4597−4610.

(30) van Lenthe, E.; Baerends, E.-J.; Snijders, J. G. *J. Chem. Phys.* **1994**, *101*, 9783−9792.

(31) Douglas, M.; Kroll, N. M. *Ann. Phys.* **1974**, *82*, 89−155.

(32) Hess, B. A. *Phys. Rev. A* **1986**, *33*, 3742−3748.

(33) Wolf, A.; Reiher, M.; Hess, B. A. *J. Chem. Phys.* **2002**, *117*, 9215−9226.

(34) Reiher, M. *Theor. Chem. Acc.* **2006**, *116*, 241−252.

(35) Reiher, M.; Wolf, A. *J. Chem. Phys.* **2004**, *121*, 2037−2047.

(36) Barysz, M.; Sadlej, A. J. *J. Chem. Phys.* **2002**, *116*, 2696−2704.

(37) Ilias, M.; Saue, T. *J. Chem. Phys.* **2007**, *126*, 064102.

(38) Bader, R. F. W.; Slee, T. S.; Cremer, D.; Kraka, E. *J. Am. Chem. Soc.* **1983**, *105*, 5061−5068.

(39) Scherer, W.; Eickerling, G.; Shorokhov, D.; Gullo, E.; McGrady, G. S.; Sirsch, P. *New J. Chem.* **2006**, *30*, 309−312.

(40) Cioslowski, J.; Karwowski, J. *Fundamentals of Molecular Similarity;* Kluwer Academic: New York, 2001.

(41) Bader, R. F. W.; MacDougall, P. J.; Lau, C. D. H. *J. Am. Chem. Soc.* **1984**, *106*, 1594−1605.

(42) Bader, R. F.; Essén, H. *J. Chem. Phys.* **1984**, *80*, 1943−1960.

(43) Sagar, R. P.; Ku, A. C. T.; Smith, V. H., Jr. *J. Chem. Phys.* **1988**, *88*, 4367−4374.

(44) Shi, Z.; Boyd, J. R. *J. Chem. Phys.* **1988**, *88*, 4375−4377.

(45) Chan, W.-T.; Hamilton, I. P. *J. Chem. Phys.* **1998**, *108*, 2473−2485.

(46) Bader, R. F. W.; Gillespie, R. J.; Martín, F. *Chem. Phys. Lett.* **1998**, *290*, 488−494.

(47) Ahlrichs, R.; Bär, M.; Häser, M.; Horn, H.; Klömel, C. *Chem. Phys. Lett.* **1989**, *162*, 165−169.

(48) Becke, A. D. *Phys. Rev. A* **1988**, *38*, 3098−3100.

(49) Perdew, J. P. *Phys. Rev. B* **1986**, *33*, 8822−8824.

(50) Dolg, M.; Wedig, U.; Stoll, H.; Preuss, H. *J. Chem. Phys.* **1987**, *86*, 866−872.

(51) Andrae, D.; Haeussermann, U.; Dolg, M.; Stoll, H.; Preuss, H. *Theor. Chim. Acta* **1990**, *77*, 123−141.

(52) ADF2006.01, SCM, Theoretical Chemistry, Vrije Universiteit, Amsterdam, The Netherlands. http://www.scm.com (accessed November 2006).

(53) te Velde, G.; Bickelhaupt, F.; van Gisbergen, S.; Guerra, C. F.; Baerends, E.; Snijders, J.; Ziegler, T. *J. Comput. Chem.* **2001**, *22*, 931−967.

(54) Jensen, H. J. Aa; Saue, T.; Visscher, L. with contributions from Bakken, V.; Eliav, E.; Enevoldsen, T.; Fleig, T.; Fossgaard, O.; Helgaker, T.; Laerdahl, J.; Larsen, C. V.; Norman, P.; Olsen, J.; Pernpointner, M.; Pedersen, J. K.; Ruud, K.; Salek, P.; van Stralen, J. N. P.; Thyssen, J.; Visser, O.; Winther, T. *Dirac, a relativistic ab initio electronic structure program, Release DIRAC04.0 (2004)*; http://dirac-.chem.sdu.dk (accessed September 2005).

(55) Saue, T.; Faegri, K.; Helgaker, T.; Gropen, O. *Mol. Phys.* **1997**, *91*, 937−950.

(56) Saue, T.; Helgaker, T. *J. Comput. Chem.* **2002**, *23*, 814−823.

(57) Dirac, P. A. M. *Proc. Camb. Phil. Soc.* **1930**, *26*, 376−385.

(58) Vosko, S. J.; Wilk, L.; Nusair, M. *Can. J. Phys.* **1980**, *58*, 1200−1211.

(59) Dyall, K. G. *Theor. Chem. Acc.* **2007**, *117*, 483−489.

(60) Dyall, K. G. *Theor. Chem. Acc.* **2004**, *112*, 403−409.

(61) Pou-Amerigo, R.; Merchan, M.; Nebotgil, I.; Widmark, P. O.; Roos, B. O. *Theor. Chim. Acta* **1995**, *92*, 149−181.

(62) Partridge, H. *J. Chem. Phys.* **1989**, *90*, 1043−1047.

(63) Dunning, T. H. *J. Chem. Phys.* **1989**, *90*, 1007−1023.

(64) Werner, H.-J.; Knowles, P. J.; Lindh, R.; Schütz, M. et al. Molpro 2006.2, a package of ab initio programs.

(65) Reiher, M.; Wolf, A. *J. Chem. Phys.* **2004**, *121*, 10945−10956.

(66) Katan, C.; Rabiller, P.; Lecomte, C.; Guezo, M.; Oison, V.; Souhassou, M. *J. Appl. Crystallogr.* **2003**, *36*, 65−73.

(67) Wolfram Research, Inc. *Mathematica Version 5.2;* Wolfram Research, Inc.: Champaign, IL, 2005.

(68) Presnitz, M.; Mayer, F.; Herz, V.; Eickerling, G.; Scherer, W. "calc.lap.nb", Universität Augsburg (Lehrstuhl CPM), 2007 Mathematica Script for the Processing of Volume Data (Calculation of the Laplacian Field).

(69) Reiher, M. Ph.D. Thesis, University of Bielefeld, 1998.

(70) Andrae, D.; Reiher, M.; Hinze, J. *Int. J. Quantum Chem.* **2000**, *76*, 473−499.

(71) Pörschke, K. R.; Yi-Hung, T.; Krüger, C. *Angew. Chem., Int. Ed. Engl.* **1985**, *24*, 323−324.

(72) Pilme, J.; Silvi, B.; Alikhani, M. E. *J. Phys. Chem. A* **2005**, *109*, 10028−10037.

(73) Schager, F.; Bonrath, W.; Pörschke, K. R.; Kessler, M.; Krüger, C.; Seevogel, K. *Organometallics* **1997**, *16*, 4276−4286.

(74) Massera, C.; Frenking, G. *Organometallics* **2003**, *22*, 2758−2765.

(75) Coppens, P. *Acta Crystallogr., Sect. A: Found. Crystallogr.* **1984**, *A40*, 184−195.

(76) Benabicha, F.; Pichon-Pesme, V.; Jelsch, C.; Lecomte, C.; Khmou, A. *Acta Crystallogr., Sect. B: Struct. Sci.* **2000**, *B56*, 155−165.

(77) Dittrich, B.; Flaig, R.; Koritsanszky, T.; Krane, H.-G.; Morgenroth, W.; Luger, P. *Chem. Eur. J.* **2000**, *6*, 2582−2589.

(78) Scherer, W.; Eickerling, G.; Tafipolsky, M.; McGrady, G. S.; Sirsch, P.; Chatterton, N. P. *Chem. Commun. (Cambridge)* **2006**, 2986−2988.

(79) Rohrmoser, B.; Eickerling, G.; Presnitz, M.; Scherer, W.; Eyert, V.; Hoffmann, R.-D.; Rodewald, U. C.; Vogt, C.; Pöttgen, R. *J. Am. Chem. Soc.* **2007**, *129*, 9356−9365.

(80) Gatti, C.; McDougall, P. J.; Bader, R. W. F. *J. Chem. Phys.* **1987**, *88*, 3792−3804.

(81) Shi, Z.; Boyd, J. *J. Chem. Phys.* **1988**, *88*, 4375−4377.

(82) McGrady, G. S.; Haaland, A.; Verne, H. P.; Volden, H. V.; Downs, A. J.; Shorokhov, D.; Eickerling, G.; Scherer, W. *Chem. Eur. J.* **2005**, *11*, 4921−4934.

(83) Volkov, A.; Abramov, Y.; Coppens, P.; Gatti, C. *Acta Crystallogr., Sect. A: Found. Crystallogr.* **2000**, *A56*, 332−339.

(84) Henn, J.; Ilge, D.; Leusser, D.; Stalke, D.; Engels, B. *J. Phys. Chem. A* **2004**, *108*, 9442−9452.

CT7001573